

# Vibrational Spectrum and Thermal Conductivity of Rare-Earth Semiconducting Erbium Nitride Thin Films

Krithika Upadhyya, Rajendra Kumar, Qinshu Li, Bo Sun, and Bivas Saha\*

Rare-earth semiconducting mononitrides (RENs) are an emerging class of materials due to their unique electronic and magnetic properties originating from strongly localized  $4f$  orbitals. Erbium nitride (ErN) is one of the most promising REN and attracts significant interest for spintronics, thermoelectric, and Gifford–McMahon cryo-cooler applications. However, despite such progress, growth and characterization of the physical properties of ErN are rather challenging due to its propensity for oxidation, and no report on its thermal transport properties exists to date. Recently, high-quality ErN thin films are deposited and are stabilized in ambient with thin capping layers. Herein this letter, first-principles density functional perturbation theory to model the vibrational spectrum of ErN is utilized and the calculations with the phonon frequency measurements with inelastic Raman spectroscopy are verified. Consistent with its polar dielectric nature, ErN exhibits a longitudinal-optical transverse-optical phonon mode splitting at the  $\Gamma$ -point with a separation of  $333\text{ cm}^{-1}$ . Time-domain thermoreflectance is used to measure the low-temperature (80–300 K) thermal conductivity of ErN films. At room temperature, ErN films exhibit a low thermal conductivity of  $1.16 \pm 0.15$  and  $2 \pm 0.2\text{ W mK}^{-1}$  on (001) MgO and (0001)  $\text{Al}_2\text{O}_3$  substrates, respectively, making them attractive for thermoelectrics and thermal barrier coating applications.

## 1. Introduction

Rare-earth semiconducting mononitrides (RENs) crystallize in the rock salt structure with octahedral bonding coordination and exhibit distinct electronic, optical, and magnetic properties that are attractive for a host of modern device applications.<sup>[1–3]</sup> Due to the presence of partially filled and highly localized  $4f$  orbitals, RENs are ferromagnetic and explored extensively for spin superlattices and spintronic devices.<sup>[4,5]</sup> The inclusion of rare-earth elements in nonmagnetic semiconductors can also add spin degrees of freedom that lead to their dilute magnetic semiconducting properties for spin-based information processing.<sup>[6,7]</sup> Erbium nitride (ErN) is one of the most promising REN and is intensely studied to harness its riveting properties in device applications. ErN is ferromagnetic below a Curie temperature of 6 K and exhibits a lattice constant of  $4.85\text{ \AA}$ .<sup>[8–10]</sup> ErN micron-sized particles have already been commercialized for Gifford–McMahon (GM) cryo-coolers that

show a very high cooling power due to the large cryogenic temperature-specific heat of ErN.<sup>[11]</sup> Even though research on ErN has been gaining attention in the last few years, Er-doped semiconductors have been studied for over 20 years for various applications. For example, due to the intra- $4f$  electronic transitions, Er-doped semiconductors such as GaN,<sup>[12,13]</sup> InGaN,<sup>[14]</sup> Si,<sup>[15]</sup> ZnO,<sup>[16]</sup> etc. exhibit emission at the retina-safe, fiber-optical telecommunication window of  $1.54\text{ }\mu\text{m}$  that is explored for the use in solid-state lasers, amplifiers, and light-emitting devices.<sup>[17,18]</sup> Er-doping in Si-based fiber amplifiers,<sup>[19]</sup> GaN-based gain medium for high-power lasers,<sup>[20]</sup> InGaN-based light-emitting diodes and electroluminescent devices,<sup>[21]</sup> and YAG lasers<sup>[22]</sup> stand out in their optoelectronic advancement point of view. In addition to this, recently, Er-implanted Si films have been studied as the potential candidates to develop quantum applications.<sup>[23]</sup>

However, experimental research on optical, thermal, and electronic properties of ErN is relatively scarce despite such progress due to its affinity toward oxygen that limits most meaningful studies of its physical properties. In one of the earliest reports in the 1960s, fine powders and dense specimens of nonstoichiometric ErN were synthesized, and an optical bandgap between 2.40 and 2.78 eV was measured.<sup>[1]</sup> Electrical measurements also showed metallic-like transport in such bulk specimens due to large carrier concentrations arising from nitrogen vacancies.


K. Upadhyya, R. Kumar, B. Saha  
Chemistry and Physics of Materials Unit  
Jawaharlal Nehru Centre for Advanced Scientific Research  
Bangalore 560064, India  
E-mail: bsaha@jncasr.ac.in

K. Upadhyya, R. Kumar, B. Saha  
International Centre for Materials Science  
Jawaharlal Nehru Centre for Advanced Scientific Research  
Bangalore 560064, India

K. Upadhyya, B. Saha  
School of Advanced Materials (SAMat)  
Jawaharlal Nehru Centre for Advanced Scientific Research  
Bangalore 560064, India

Q. Li, B. Sun  
Tsinghua-Berkeley Shenzhen Institute  
Tsinghua University  
Shenzhen 518055, China

B. Sun  
Guangdong Provincial Key Laboratory of Thermal Management  
Engineering & Materials  
Tsinghua Shenzhen International Graduate School  
Shenzhen 518055, China

 The ORCID identification number(s) for the author(s) of this article can be found under <https://doi.org/10.1002/pssr.202200029>.

DOI: 10.1002/pssr.202200029

More recently, ErN bulk crystals are synthesized with the physical vapor transport method on tungsten foils at high temperatures (1620–1770 °C).<sup>[9]</sup> Diffraction studies showed that the ErN crystals preferred (001) oriented growth following the predominant tungsten sheet orientation and deviated from stoichiometry. Photoemission measurement on the ErN crystals though initially had suggested a direct bandgap of  $\approx 1$  eV, subsequent low-temperature PL measurement showed a minimum bandgap of  $\approx 2.4$  eV, which is consistent with the reports in the 1960s.<sup>[1,10]</sup> PL measurements also showed the presence of two valence bands and two conduction bands at the  $\Gamma$ -point that are separated by 0.15 and 0.34 eV, respectively, in ErN.<sup>[10]</sup>

While the experimental research on thin-film ErN has been inadequate, first-principles modeling analysis initially suggested ErN be a zero-gap semiconductor with the top of the valence band situated at the  $\Gamma$ -point, and the bottom of the conduction band located at the X-point of the Brillouin zone, respectively.<sup>[2]</sup> However, as traditional density-functional theory (DFT) calculations underestimate the bandgap of semiconductors, such predictions are not surprising. Subsequently localized spin-density approximation calculations with Hubbard U-corrections (with U applied at the Er-4*f* orbitals) showed a direct bandgap of 0.97 eV and an indirect gap between 0.53 and 0.65 eV depending on the magnetic transitions.<sup>[4]</sup> However, since the valence band edge in ErN is expected to be dominated by Er-5*d* and N-2*p* states, the inclusion of Hubbard U correction on Er-4*f* orbitals is unlikely to result in an appropriate bandgap. Furthermore, quasiparticle self-energy corrections with DFT revealed a bandgap of  $\approx 0.2$  eV in ErN.<sup>[4]</sup>

Though such progress on understanding the electronic structure of ErN is noteworthy, when it comes to the analysis of the thermal transport properties, very few reports exist to date. The thermal conductivity of bulk ErN has been measured at cryogenic temperatures from 10 to 80 K.<sup>[24]</sup> In addition, theoretical assessments have been made on the elastic constants, ultrasonic velocity, and anisotropic thermal conductivity<sup>[25]</sup> of Er-pnictides. Moreover, though the Raman spectroscopy is used to measure phonon frequencies in bulk ErN and frozen phonon calculations are performed to calculate the phonon spectrum at the  $\Gamma$ , L, and X points,<sup>[9]</sup> calculation of the full-phonon dispersion, phonon densities of states (DOSs), and other important vibrational spectrum-related properties such as Born effective charge are still missing.<sup>[26]</sup>

Recently, we have developed high-quality textured ErN thin films<sup>[27]</sup> on (001) MgO and (0001) Al<sub>2</sub>O<sub>3</sub> substrates with ultra-high vacuum (UHV) magnetron sputtering at a base pressure of  $1 \times 10^{-9}$  Torr. ErN films are also stabilized at ambient conditions by depositing a thin layer of AlN and/or TiN in situ on top during the deposition process that prevents its exposure to moisture.<sup>[27]</sup> The columnar ErN films grow on both the substrates with (002) and (111) orientations and exhibit sharp interfaces.<sup>[27]</sup> Electrical measurements show that the ErN films are degenerated with a high carrier concentration in the  $10^{20}$ – $10^{21}$  cm<sup>-3</sup> range and exhibit low mobility of 3–4 cm<sup>2</sup> Vs<sup>-1</sup>.<sup>[27]</sup> Synchrotron-radiation photoemission measurements with ultraviolet photoelectron spectroscopy also showed a valence band maximum and Fermi energy difference of  $\approx 2.3$  eV in ErN.<sup>[28]</sup> Further, DFT calculations with Heyd–Scuseria–Ernzerhof (HSE) hybrid functional and GGA + U Hubbard corrections with

the onsite potential (U) incorporated at the Er-5*d* states are found to capture the experimental band structure well. Both longitudinal and transverse conduction band effective mass and volume deformation potentials are further calculated from the band structure to understand the transport properties better. Temperature-dependent thermoelectric measurements show that ErN films exhibit a moderately high Seebeck coefficient of  $-72.6 \mu\text{V K}^{-1}$  at 640 K and thermoelectric power factor of  $0.44 \times 10^{-3} \text{ W mK}^2$  at 486 K that upholds the possibility to use ErN in thermoelectric energy conversion, provided that the thermal conductivity is small.<sup>[27]</sup> Therefore, with the motivation to understand the fundamental nature of ErN's vibrational spectrum and to determine its suitability for thermoelectric applications, in this work, we present detailed first-principles density-functional perturbation theory (DFPT) modeling of ErN's phonon dispersion, phonon frequencies determined with Raman spectroscopy, and temperature-dependent thermal conductivity.

## 2. Results and Discussion

The phonon dispersion of ErN (see **Figure 1**) shows the presence of three acoustic and three optical phonon modes consistent with its two-atom unit cell. Acoustic phonons correspond to the Er vibrations due to their heavy mass, while the nitrogen atom vibrations dominate optical modes in ErN. The highest frequencies of the longitudinal-acoustic (LA) and transverse-acoustic (TA) phonon modes at the X-point of the Brillouin zone are 174 and 154 cm<sup>-1</sup>, and L-points of the Brillouin zone are 175 and 83 cm<sup>-1</sup>, respectively, which is much smaller than the corresponding phonon frequencies in ScN. From the slope of the acoustic phonon modes, a sound velocity of 885 and 501 ms<sup>-1</sup> is calculated for the LA and TA phonon modes, respectively, which is much smaller than ScN's sound velocities. Further, a Debye temperature of 314 K is calculated from the simulated vibrational spectrum, which is much lower than semiconducting transition metal nitride such as ScN, but comparable to the metallic nitrides such as HfN.<sup>[29]</sup> Recently, Rasul et al.<sup>[30]</sup> have calculated the Debye temperature of Er-pnictides using Gibbs2 code and found a Debye temperature of 405 K for ErN, which is slightly higher compared to our calculated Debye temperature of ErN.

In terms of the optical phonon, the most crucial feature is the splitting of the longitudinal-optical (LO) and transverse-optical (TO) phonon modes at the  $\Gamma$ -point due to long-range dipole-dipole interactions. The amount of the LO–TO splitting ( $\Delta\omega_{\text{LO-TO}}$ ) in ErN is 333 cm<sup>-1</sup>, which is very close to the  $\Delta\omega_{\text{LO-TO}}$  of another pnictide semiconductor, ScN. Such a comparable amount of LO–TO splitting in ErN and ScN represents their similar high-frequency dielectric constant ( $\epsilon^\infty$ ) and Born effective charges. While in ErN, our calculation suggests an  $\epsilon^\infty$  and Born effective charge of 14.0 and 4.72, respectively, previous DFPT calculations have shown corresponding values in ScN to be 12.9 and 4.35.<sup>[29]</sup> At the  $\Gamma$ -point, the LO mode has a maximum frequency of 489 cm<sup>-1</sup>, while at the L-point, the LO mode has the highest frequency of 559 cm<sup>-1</sup>. The phonon DOSs clearly show (see **Figure 1**) the splitting of the LO and TO modes with LO modes occupying the higher frequency range.

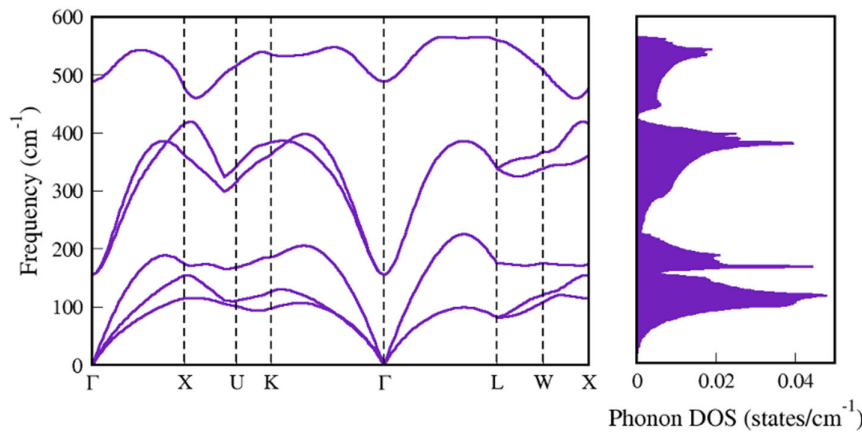


**Figure 1.** Phonon-dispersion curve (LHS) and the corresponding phonon densities of states (DOSs) (RHS) of ErN, calculated using first-principles density-functional perturbation theory (DFPT) calculations. Consistent with its polar dielectric nature, ErN exhibits a longitudinal-optical (LO) and transverse-optical (TO) splitting at the  $\Gamma$ -point.

Raman spectroscopy measurements are performed on ErN films deposited on (001) MgO and (0001)  $\text{Al}_2\text{O}_3$  substrates to verify the phonon dispersion calculations. Due to the resonant enhancement caused by the red laser, whose wavelength is closer to the bandgap of ErN, Raman peaks obtained with the red laser source were more prominent and intense than the one obtained with the green laser source. As a result, Raman spectra from the red laser source only are plotted along with the calculated phonon DOS in **Figure 2**. As ErN exhibits a rock salt crystal structure with a space group of 225, the first-order Raman signature is symmetry forbidden. However, defects lift the  $q$ -selection rules, and a second-order Raman spectrum is observed that corresponds to a weighted one phonon DOSs in ErN. Comparing the experimentally measured Raman spectrum with the calculated phonon DOS shows that

the spectral features match very well with one another. The highest frequency band is between  $470$  and  $600\text{ cm}^{-1}$  with a peak at  $\approx 553.60\text{ cm}^{-1}$  corresponding to the LO lattice vibration, as shown by the calculations. Similarly, the spectral width of the TO phonon mode spanning from  $\approx 217.87$  to  $449.5\text{ cm}^{-1}$  is in good agreement with the DFPT analysis. The peak at  $553.60\text{ cm}^{-1}$  that corresponds to the LO phonon modes at the L-point of the Brillouin zone was reported previously on micron-sized bulk ErN crystals<sup>[9]</sup> and on ErN films.<sup>[26]</sup> Using frozen-phonon approach, Granville et al.<sup>[26]</sup> have calculated LO (L) phonon mode frequency at  $592\text{ cm}^{-1}$  and compared with the experimental observed mode at  $\approx 550\text{ cm}^{-1}$ . However, our calculated value of LO (L) phonon mode frequency matches better with the experimentally measured Raman frequency. The center of the TO band is located at  $\approx 326\text{ cm}^{-1}$  that is also most likely contributed by the L-point. Note that the LO phonon mode frequencies in ErN are about  $110\text{ cm}^{-1}$  smaller than the LO phonon mode observed in the Raman spectrum of ScN.<sup>[31]</sup> Since the LO modes are primarily nitrogen atom vibrations, it highlights a stiffer force constant in ErN compared to ScN.

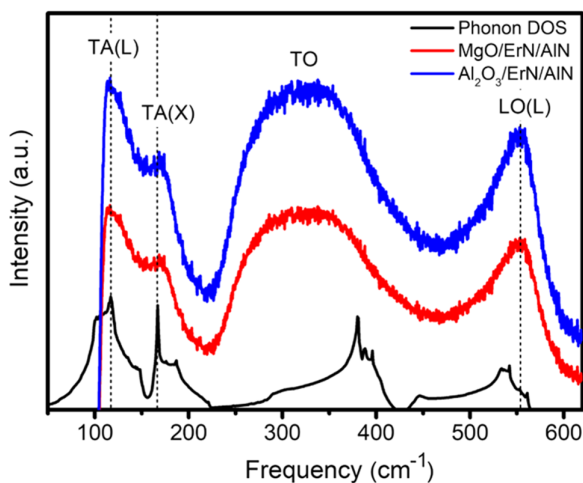


**Figure 2.** Raman spectra of ErN on MgO (red) as well as  $\text{Al}_2\text{O}_3$  (blue) substrate, recorded using incident laser wavelength of  $630\text{ nm}$ , are plotted along with the phonon DOS as the reference. Calculated DOS matches well with an experimentally determined second-order Raman spectrum corresponding to a weighted one phonon DOSs in ErN.

Having determined the Raman spectrum, we have performed the temperature-dependent thermal conductivity measurements with a time-domain thermoreflectance (TDTR) technique<sup>[32,33]</sup> (see Supporting Information for details). The measured total thermal conductivity,  $\kappa$ , is shown in **Figure 3**. We also calculated the electronic contribution to the thermal conductivity  $K_e$  using Wiedemann–Franz law. We can see that  $K_e$  is small and the dominate heat carrier in ErN films is phonon. The total thermal conductivity,  $\kappa$ , of ErN films deposited on (001) MgO and (0001)  $\text{Al}_2\text{O}_3$  substrates shows a typical thermal conductivity dominated by phonon–boundary scattering. A fitting (green solid line) of the decreasing part of the thermal conductivity with  $\kappa = AT^\alpha$ , where  $\kappa$ ,  $T$ ,  $\alpha$ , and  $A$  are the thermal conductivity, absolute temperature, Umklapp scattering exponent, and a constant, respectively, shows an  $\alpha$  of  $-0.82$ , which is smaller than the ideal  $\alpha$  of  $-1$  for the Umklapp scattering process.<sup>[34,35]</sup> Such lower values of the Umklapp scattering exponent manifest the impure nature of semiconducting ErN with defects.

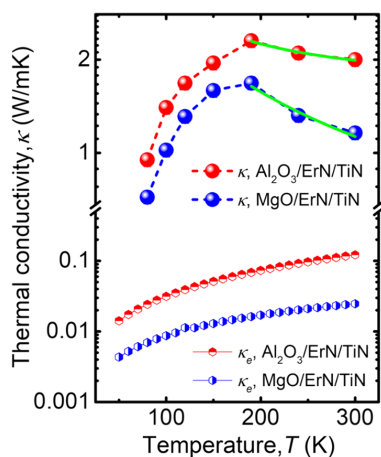


**Figure 3.** Total thermal conductivity and electron contribution to the thermal conductivity of the ErN sample on both (001) MgO (blue) and (0001) Al<sub>2</sub>O<sub>3</sub> (red) substrates are measured between  $\approx 80$  to 370 K range. The solid line drawn over the total thermal conductivity graph represents the Umklapp fitting data. Here,  $\kappa$  is the total thermal conductivity and  $\kappa_e$  is the electronic contribution to the thermal conductivity. Error bars are presented in the Supporting Information as they are not visible clearly due to the large scale.

The thermal conductivity of ErN deposited on (0001) Al<sub>2</sub>O<sub>3</sub> is higher at all temperatures compared to the thermal conductivity of ErN deposited on (001) MgO substrates. This behavior can be attributed to the increased phonon scattering caused by the smaller grain size of the ErN films deposited on (001) MgO substrate that reduces its thermal conductivity. The plan-view scanning electron microscopy (SEM) images corresponding to ErN deposited on (001) MgO as well as (0001) Al<sub>2</sub>O<sub>3</sub> substrates are presented in one of the previous works.<sup>[27]</sup> At 300 K, ErN/MgO and ErN/Al<sub>2</sub>O<sub>3</sub> films exhibit a thermal conductivity of  $1.16 \pm 0.15$  and  $2 \pm 0.2$  W mK<sup>-1</sup>, respectively, an order of magnitude smaller than ScN.<sup>[36,37]</sup> The higher atomic mass of Er that leads to smaller acoustic phonon frequencies results in such low thermal conductivity in ErN. Wiedemann–Franz law is used further to calculate the electronic contribution to the total thermal conductivity from the electrical conductivity, which shows that the phonon contributions primarily dominate the total thermal conductivity of ErN.

Moreover, from our previous study, we found out that ErN shows the potential to act as an efficient thermoelectric material by exhibiting a Seebeck coefficient of  $-43.2 \mu\text{V K}^{-1}$  and thermoelectric power factor of  $0.26 \times 10^{-3}$  W mK<sup>-2</sup> on (0001) Al<sub>2</sub>O<sub>3</sub> and  $-39.9 \mu\text{V K}^{-1}$  and  $0.34 \times 10^{-3}$  W mK<sup>-2</sup> on (001) MgO substrates at 300 K. Substituting these values in the thermoelectric figure-of-merit calculations, the  $zT$  of ErN is calculated to be 0.04 and 0.08, respectively. While these values are rather small, note that the values are not obtained at the maximum power factor values due to limitations on the high-temperature thermal conductivity measurements. Hence, further research on the measurement of high-temperature thermal conductivity as well as the growth of better crystal quality ErN, having better control over impurities and lower carrier concentration and mobility, should lead to its higher thermoelectric efficiencies.

### 3. Conclusion

In conclusion, a comprehensive first-principles DFPT modeling of the vibrational spectrum of ErN coupled with the experimental measurement of the Raman spectrum and the thermal conductivity is presented. Low-temperature thermal conductivity of textured highly crystalline ErN thin films deposited on (001) MgO and (0001) Al<sub>2</sub>O<sub>3</sub> substrates with UHV magnetron sputtering shows a low thermal conductivity of  $1.16 \pm 0.15$  and  $2 \pm 0.2$  W mK<sup>-1</sup> at 300 K, respectively. Defect-induced second-order Raman spectrum matches well with the calculated densities of phononic states. Phonon dispersion calculations clearly show an LO–TO splitting at the  $\Gamma$ -point of the Brillouin zone due to the polar semiconductor nature of ErN. Determination of the vibrational properties and thermal conductivity of ErN mark significant progress in the quest to design ErN-based thermoelectric, optoelectronic, and spintronic devices.

### 4. Experimental Section

**Simulation Details:** DFPT calculations were performed with plane-wave self-consistent field (PWSCF) implementations of the DFT with a generalized gradient approximation of the exchange–correlation energy and Perdew–Burke–Ernzerhof pseudopotentials generated using the projector augmented-wave (PAW) method. The Brillouin zone integration was carried out on a  $16 \times 16 \times 16$  mesh of  $k$ -points, while the force constant matrix was obtained on a  $4 \times 4 \times 4$   $q$ -point grid (see Supporting Information for details). Dynamical matrices at any arbitrary wave vector were subsequently obtained from Fourier transform-based interpolations.

**Experimental Details:** For Raman spectroscopy and thermal conductivity measurements, ErN films were deposited on (001) MgO and (0001) Al<sub>2</sub>O<sub>3</sub> substrates with UHV DC magnetron sputtering at a substrate temperature of 800 °C (see Supporting Information for details), with similar growth conditions as in our previous work.<sup>[27]</sup> Raman spectroscopy measurements were performed with a Horiba Raman spectrometer in the backscattering geometry at room temperature with an incident laser excitation wavelength of 630 nm (1.96 eV) and 540 nm (2.3 eV), respectively. The TDTR measurements were performed with a Ti: Sapphire laser with a repetition rate of 80 MHz and a modulation frequency of 10.1 MHz. The interface resistance between the TiN and the ErN was included in the model. A cryostat operating at  $10^{-6}$  Torr was used for the low-temperature thermal conductivity measurements (see Supporting Information for detailed TDTR method and data fitting). For Raman spectroscopy measurements, a thin 3 nm AlN capping layer was used on top of the 300 nm ErN film to protect it from oxidation. For the TDTR measurements, in contrast, the 100 nm TiN layer was deposited in situ on the 464 nm ErN layer on MgO and 520 nm ErN layer on Al<sub>2</sub>O<sub>3</sub> substrates, respectively, which acted both as a transducer and oxidation protective layer.

### Supporting Information

Supporting Information is available from the Wiley Online Library or from the author.

### Acknowledgements

K.U. and R.K. contributed equally to this work. K.U., R.K., and B.S. acknowledge support from the International Centre for Materials Science (ICMS) and Sheikh Saqr Laboratory (SSL) of the Jawaharlal Nehru Centre for Advanced Scientific Research (JNCASR). B.S. acknowledges the Science and Engineering Research Board (SERB) of the Government of India, Start-Up Research grant SRC/2019/000613 for partial financial support.



Q.L. and B.S. acknowledge the support of Guangdong Natural Science Foundation (No. 2019A1515010868), the National Natural Science Foundation of China (No. 12004211), the Shenzhen Science and Technology Program (No. RYX20200714114643187), and Tsinghua Shenzhen International Graduate School (No. QD2021008N).

## Conflict of Interest

The authors declare no conflict of interest.

## Data Availability Statement

The data that support the findings of this study are available from the corresponding author upon reasonable request.

## Keywords

density functional perturbation theory, ErN, phonon dispersion, Raman spectroscopy, rare earth pnictide, thermal conductivity

Received: January 25, 2022

Revised: February 25, 2022

Published online: March 8, 2022

- 
- [1] N. Sclar, *J. Appl. Phys.* **1964**, 35, 1534.  
 [2] F. Natali, B. J. Ruck, N. O. V. Plank, H. J. Trodahl, S. Granville, C. Meyer, W. R. L. Lambrecht, *Prog. Mater. Sci.* **2013**, 58, 1316.  
 [3] C.-G. Duan, R. F. Sabirianov, W. N. Mei, P. A. Dowben, S. S. Jaswal, E. Y. Tsybal, *J. Phys.: Condens. Matter* **2007**, 19, 315220.  
 [4] P. Larson, W. R. L. Lambrecht, A. Chantis, M. van Schilfgaarde, *Phys. Rev. B* **2007**, 75, 045114.  
 [5] M. A. McKay, Q. W. Wang, H. A. Al-Atabi, Y. Q. Yan, J. Li, J. H. Edgar, J. Y. Lin, H. X. Jiang, *Appl. Phys. Lett.* **2020**, 116, 171104.  
 [6] J. K. Hite, J. M. Zavada, *ECS J. Solid State Sci. Technol.* **2019**, 8, P527.  
 [7] Y.-K. Zhou, H. Asahi, *Molecular Beam Epitaxy: Materials and Applications for Electronics and Optoelectronics*, John Wiley & Sons Ltd, Chichester, UK **2019**, pp. 299–313.  
 [8] C. Meyer, B. J. Ruck, A. R. H. Preston, S. Granville, G. V. M. Williams, H. J. Trodahl, *J. Magn. Magn. Mater.* **2010**, 322, 1973.  
 [9] H. A. Al Atabi, Z. F. Al Auda, B. Padavala, M. Craig, K. Hohn, J. H. Edgar, *Cryst. Growth Des.* **2018**, 18, 3762.  
 [10] M. A. McKay, H. A. Al-Atabi, J. Li, J. H. Edgar, J. Y. Lin, H. X. Jiang, *Appl. Phys. Lett.* **2021**, 118, 131108.  
 [11] T. Nakano, S. Masuyama, Y. Hirayama, T. Izawa, T. Nakagawa, Y. Fujimoto, T. Irie, E. Nakamura, T. A. Yamamoto, *Appl. Phys. Lett.* **2012**, 101, 251908.  
 [12] D. K. George, M. D. Hawkins, M. McLaren, H. X. Jiang, J. Y. Lin, J. M. Zavada, N. Q. Vinh, *Appl. Phys. Lett.* **2015**, 107, 171105.  
 [13] Z. Y. Sun, Y. Q. Yan, T. B. Smith, W. P. Zhao, J. Li, J. Y. Lin, H. X. Jiang, *Appl. Phys. Lett.* **2019**, 114, 222105.  
 [14] N. Woodward, V. Dierolf, J. Y. Lin, H. X. Jiang, J. M. Zavada, *Opt. Mater.* **2011**, 33, 1059.  
 [15] T. Dejima, R. Saito, S. Yugo, H. Isshiki, T. Kimura, *J. Appl. Phys.* **1998**, 84, 1036.  
 [16] S. Bhatia, N. Verma, R. K. Bedi, *Opt. Mater.* **2016**, 62, 392.  
 [17] R. Dahal, C. Ugolini, J. Y. Lin, H. X. Jiang, J. M. Zavada, *Appl. Phys. Lett.* **2009**, 95, 111109.  
 [18] D. T. X. Thao, C. A. J. Ammerlaan, T. Gregorkiewicz, *J. Appl. Phys.* **2000**, 88, 1443.  
 [19] A. W. Naji, B. A. Hamida, X. S. Cheng, M. A. Mahdi, S. Harun, S. Khan, W. F. Al-Khateeb, A. A. Zaidan, B. B. Zaidan, H. Ahmad, *Int. J. Phys. Sci.* **2011**, 6, 4674.  
 [20] Z. Y. Sun, H. L. Gong, Y. Q. Yan, T. B. Smith, J. Li, J. Y. Lin, H. X. Jiang, *J. Appl. Phys.* **2020**, 127, 243107.  
 [21] R. Dahal, C. Ugolini, J. Y. Lin, H. X. Jiang, J. M. Zavada, *Appl. Phys. Lett.* **2010**, 97, 141109.  
 [22] N. Ter-Gabrielyan, V. Fromzel, X. Mu, H. Meissner, M. Dubinskii, *Opt. Lett.* **2013**, 38, 2431.  
 [23] M. A. Hughes, H. Li, N. Theodoropoulou, J. D. Carey, *Sci. Rep.* **2019**, 9, 19031.  
 [24] S. Nishio, T. Nakagawa, T. Arakawa, N. Tomioka, T. A. Yamamoto, T. Kusunose, K. Niihara, T. Numazawa, K. Kamiya, *J. Appl. Phys.* **2006**, 99, 08K901.  
 [25] V. Bhalla, D. Singh, *Indian J. Pure Appl. Phys.* **2016**, 54, 40.  
 [26] S. Granville, C. Meyer, A. R. H. Preston, B. M. Ludbrook, B. J. Ruck, H. J. Trodahl, T. R. Paudel, W. R. L. Lambrecht, *Phys. Rev. B* **2009**, 79, 054301.  
 [27] K. Upadhyaya, V. Bhatia, A. I. Kamalasanan Pillai, M. Garbrecht, B. Saha, *Appl. Phys. Lett.* **2021**, 118, 132103.  
 [28] K. Upadhyaya, R. Kumar, M. Baral, S. Tripathi, S. N. Jha, T. Ganguli, B. Saha, *Phys. Rev. B* **2022**, 105, 075138.  
 [29] B. Saha, J. Acharya, T. D. Sands, U. V. Waghmare, *J. Appl. Phys.* **2010**, 107, 033715.  
 [30] M. N. Rasul, M. Mehmood, A. Hussain, A. Manzoor, M. A. Khan, F. Iqbal, *Comput. Condens. Matter* **2021**, 27, e00540.  
 [31] K. C. Maurya, B. Biswas, M. Garbrecht, B. Saha, *Phys. Status Solidi RRL* **2019**, 13, 1900196.  
 [32] D. G. Cahill, *Rev. Sci. Instrum.* **2004**, 75, 5119.  
 [33] B. Sun, Y. K. Koh, *Rev. Sci. Instrum.* **2016**, 87, 064901.  
 [34] B. Qiu, H. Bao, G. Zhang, Y. Wu, X. Ruan, *Comput. Mater. Sci.* **2012**, 53, 278.  
 [35] G. A. Slack, R. A. Tanzilli, R. O. Pohl, J. W. Vandersande, *J. Phys. Chem. Solids* **1987**, 48, 641.  
 [36] S. Kerdsonpanya, B. Sun, F. Eriksson, J. Jensen, J. Lu, Y. K. Koh, N. Van Nong, B. Balke, B. Alling, P. Eklund, *J. Appl. Phys.* **2016**, 120, 215103.  
 [37] S. Kerdsonpanya, O. Hellman, B. Sun, Y. K. Koh, J. Lu, N. Van Nong, S. I. Simak, B. Alling, P. Eklund, *Phys. Rev. B* **2017**, 96, 195417.